UNIVERSITY OF BIRMINGHAM
University of Birmingham Research at Birmingham

First-principles calculations of intrinsic stacking fault energies and elastic properties in binary nickel alloys

Breidi, Abed; Allen, Joshua; Mottura, Alessandro

Document Version
Publisher's PDF, also known as Version of record

[Link to publication on Research at Birmingham portal](#)

Full length article

First-principles calculations of intrinsic stacking fault energies and elastic properties in binary nickel alloys

A. Breidi *, J.D.T. Allen, A. Mottura

University of Birmingham, School of Metallurgy and Materials, Elms Rd, Birmingham, England, B15 2TT, United Kingdom

ARTICLE INFO

ABSTRACT

Density Functional Theory based first-principles calculations were performed to determine the compositional variation of the intrinsic stacking fault energy (ISFE) and the elastic properties in Ni-based concentrated alloys, modeled as chemically disordered solid solutions. Most of the solutes reduce the ISFE of the nickel matrix, where elements characterized by half or near half *d*-band filling (Mo, V, Tc, Ru, Cr, Os, Re, W) are predicted to produce the highest decline rates of the ISFE. The decisive role played by chemical short range order in determining the ISFE in Ni-based multicomponent *γ* phase alloys is discussed. Osmium is predicted to improve the elastic moduli of the fcc Ni matrix. Osmium high ISFE decline rate and excellent elastic moduli make it a potent element improving the mechanical properties of Ni-based super and multi-principal element alloys. This role seems to have been identified in a recently developed osmium-containing Ni-based superalloy, see Wei *et al.* (2022).

1. Introduction

In an aeroengine, the turbine blading is machined to a strict tolerance relative to the engine casing. During service, the blades are subjected to high temperatures and stress conditions which cause plastic strain to accumulate over time through the creep mechanism. This effect is very important as excessive creep deformation will cause the blades to fail while in service. This demonstrates the need for creep-resistant materials, such as Ni-based superalloys, having the ability to prolong the lifetime of this turbine component.

Ni-Based superalloys are highly significant to the hot sections of jet engines and industrial gas turbines due to their exceptional high temperature mechanical properties. These properties are derived from a two phase γ/γ' microstructure, where the γ' phase is L1$_2$-Ni$_3$Al in precipitate form and the γ phase is a matrix of fcc-Ni. The γ' phase results in order strengthening and dislocation locks forming in the precipitates due to thermal activation, which is the reason for the Yield Stress Anomaly (YSA) of superalloys.

Creep strengthening in Ni-based alloys emerges from precipitation hardening due to the γ' phase and from solid-solution strengthening due to solutes partitioning to the γ matrix. The γ' precipitates, stabilized and solid-solution strengthened through adding Al, Ti, Ta, Nb, and V, has a prominent influence on the creep resistance of Ni-based alloys [1]. These precipitates act as barriers hindering the dislocation motion within the crystal, thereby reducing strongly creep deformation. It has been shown that an increasing fraction of γ' precipitates increases creep

strengthening effect, specifically an increase in life-to-rupture time and a decrease in minimum creep rate [2]. It should be mentioned that this is true at low stresses, otherwise dislocations can shear the γ' precipitates [3].

Creep deformation in pure metals such as nickel occurs *via* a combined glide-climb process at temperatures where vacancies become mobile. When a gliding dislocation is pinned, it can be released *via* a vacancy-mediated-climb and continue gliding. Dislocation glide is then responsible for the greater part of creep deformation. Recovery-controlled creep models of pure metals [4,5] are based on the assumption that the steady-state creep is achieved when the operating rate of dislocation multiplication equalizes that of dislocation annihilation, yielding subsequently a constant dislocation density. This assumption has been used to derive a law [6–8], in pure metals, describing the creep strain rate – referred to also as minimum, or steady state or secondary creep rate – dependence on the intrinsic stacking fault energy γ_{ISF}

$$\dot{\epsilon} \propto \frac{Gb}{K_B T} \left(\frac{\gamma_{\text{ISF}}}{Gb} \right)^3 \left(\frac{\sigma}{G} \right)^5 D_{\text{SD}} , \qquad (1)$$

where D_{SD}, σ, G, T, b, and K_B are the self-diffusion coefficient, applied stress, shear modulus, temperature, Burgers vector, and the Boltzman constant, respectively. Refs. [9,10] studied solid-solution strengthened materials, where it was noticed that a large number of binary alloys behave similarly to pure metals exhibiting a five-power-law dependence

---

(Eq. (1)) on the applied stress. The studied set of binary alloys included nickel as a host matrix and various solutes relevant to Ni-superalloys. This shows that effects produced by various alloying elements relevant to Ni-superalloys can be interpreted using Eq. (1) – the five power law of secondary creep rate.

As given in Eq. (1), the secondary creep strain-rate $\dot{\epsilon}$ depends on γ_{ISF} the intrinsic stacking fault energy. In an fcc metal, a perfect dislocation $a/2\langle 110 \rangle$ gliding in $\{\bar{1}11\}$ plane dissociates into two Shockley partial dislocations separated by an intrinsic planar stacking fault of width d. Electron microscopy showed that the dissociation obeys this reaction form

$$a/2\langle 110 \rangle \{\bar{1}11\} \rightarrow a/6\langle 211 \rangle \{\bar{1}11\} \tag{2}$$
$$+$$
$$a/6\langle 12\bar{1} \rangle \{\bar{1}11\} \,,$$
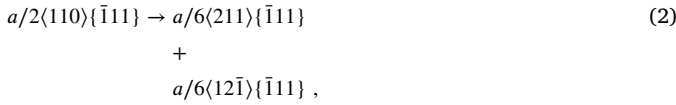
ISF energy (J m^{-2} or N m^{-1}) is an attractive force per unit length (N m^{-1}) acting on the two dissociated Shockley partial dislocations, $a/6\langle 211 \rangle \{\bar{1}11\}$ and $a/6\langle 12\bar{1} \rangle \{\bar{1}11\}$, tending to pull them together.

Screw portions of the perfect dislocation $a/2\langle 110 \rangle$ can circumvent obstacles such as precipitates through a cross-slip mechanism, thereby facilitating creep deformation. In most cases, unless the γ_{ISF} is very high where dissociation is not favorable, a perfect dislocation in an fcc metal exists in an extended dislocation form as shown in Eq. (2). As a result, a cross-slip cannot occur because $a/6\langle 211 \rangle$ vector lies in only one $\{111\}$ plane and thus an individual Shockley partial cannot cross slip. Therefore, the extended dislocation is constrained to glide in the $\{111\}$ plane of its fault. It follows that cross-slip would be difficult to occur in significantly low ISF energy metals due to constriction difficulties, which is advantageous as this impedes gliding dislocations from by-passing obstacles inducing thus a creep-resisting effect. It is important to mention within this context that a large elastic shear modulus G can cause the dissociation of the perfect dislocation even if the ISF energy is high. This is due to the fact that the dislocation dissociation width is directly proportional to G and inversely proportional to γ_{ISF} as given in the theory of elasticity [11,12]. Thus a reasonably big shear modulus is equally advantageous to a significantly low ISF energy because it prevents the two Shockley partials to constrict locally. Hence, when considering the effect of alloying on γ_{ISF}, it is crucial as well to monitor the change in G of the fcc Ni matrix.

Therefore widely spaced Shockley partials arising from low ISF energies and/or reasonably big shear moduli are advantageous to high-temperature applications, as they produce a creep resistance effect. It has long been established that adding alloying elements to most base metals can strongly lower their ISF energy [13]. Concerning solid-solution strengthened nickel, a correlation between the normalized steady-state creep rate and the γ_{ISF} is known to exist [6]; a decrease in the ISF energies, upon adding transition metal elements, was associated with a decrease in the steady-state creep rate. Earlier experimental investigations [14,15] have demonstrated the profound effect of solutes on the creep resistance of polycrystalline nickel. Adding Cr or Co to the nickel matrix induced a substantial decrease in the secondary creep strain-rate, yielding a desirable solid-solution hardening effect. The results [14,15] also showed that creep-strengthening increment correlates strongly with the atomic-size mismatch between nickel and the solute, and with the concentration of solute added.

Given the important role of ISF energy in affecting the mechanical properties of Ni-based alloys, it is essential to establish quantitatively its compositional variation across a wide range of 3d, 4d, and 5d solutes. This systematic study enables comparing the effect of solute's type on altering the ISFE of fcc nickel and subsequently correlating the highest decline rate in ISFE with the solute's position in the periodic table. The individual compositional variations in the ISFE helps understanding the role of elements already used in state-of-the-art Ni-base superalloys and identifying other elements that induce substantial ISFE decline rates but have not received focus in the past. To this end, solutes typically

used in various generations of single and polycrystalline nickel-base superalloys are considered, specifically, Ti, V, Cr, Fe, Co, Nb, Mo, Ru, Ta, W, and Re. To see the trend of γ_{ISF} variation across a wide range of 3d, 4d, and 5d band series, Platinum group metals (Pt, Pd, Rh, Ir, Os) and other elements (Mn, Cu, Zn, Tc, Au) are also considered.

There exist different computational studies in the literature that calculate the ISFE in Ni-based fcc alloys, however, the focus is either on a single or a few binary systems. In this first-principles study, we employ Density-functional theory (DFT) based calculations in conjunction with the axial Ising model (AIM) [16] and using big supercells to examine the compositional variation of the ISFE in fcc Ni-X binaries for a wide range of 3d, 4d, and 5d X solutes, where the alloys are modeled as random solid solutions. The solute composition range in each alloy is restricted to its low-medium temperature solubility limit in the respective experimental phase diagram. The structural energetics relevant to ISFE calculations of high temperature solubility compositions can be strongly affected by thermal effects, specifically, electronic, vibrational, magnetic and anharmonic energy contributions, and as a consequence 0 K calculations are not sufficient.

Similarly, big supercells have been employed to calculate the elastic constants and moduli of fcc Ni-X binaries. The solutes considered to investigate their elastic effect on fcc Ni matrix are those known to preferentially partition to the γ phase in Ni-based two phase γ/γ' superalloys excluding Cr. Specifically, Fe, W, Mo, Ta, Co, Re, and Ru; Os is also considered though it has not received much focus in Ni-superalloy research until recently [17].

We predict the ISFE compositional variation to vary strongly between the different systems, where solutes lying towards the center of the transition metal series, Mo, V, Tc, Ru, Cr, Os, Re, and W display the highest ISFE decline rates. We discuss osmium's ISFE high decline rate and known excellent elastic moduli on its potential role as a potent element improving the mechanical properties of future Ni-based multicomponent alloys. The solutes considered in the elastic study exhibit important and different effects on changing the elastic moduli of fcc Ni matrix. Though strictly speaking, the predicted change in the shear moduli is less pronounced than that in γ_{ISF}; an observation highlighting the key role played by γ_{ISF} in increasing the dislocation dissociation width of fcc Ni matrix upon alloying.

2. Methodology

2.1. Intrinsic stacking fault energy and the axial Ising model

The separation of the two Shockley partial dislocations will disrupt the $\{111\}$ planes stacking sequence *ABCABCABCABC*, introducing a ribbon of stacking fault between them. The stacking sequence of $\{111\}$ planes will be faulted between the Shockley partials and pristine outside the dislocation. This intrinsic stacking fault consists of four layers of hexagonal close-packed stacking (*ABCACABCABC*) within a face centered cubic lattice.

Experimental observations [18] of extended dislocations in thin foils have established that under stress, the dissociated dislocation $a/2\langle 110 \rangle$ glides as a pair of partials bounding the ISF ribbon where the leading partial $a/6\langle 211 \rangle$ creates the fault and the trailing one $a/6\langle 12\bar{1} \rangle$ removes it. Experimental estimates of the ISF energy γ_{ISF} have been mainly made from direct observation of the fault-ribbon width using transmission electron microscope TEM and from direct observation of the shrinkage rate of faulted prismatic loops [19]. Experimental estimates have also been reported indirectly from the temperature dependence of the flow stress of single crystals.

The magnitude of the distance d separating the two Shockley partials in Eq. (2) depends on the ISF energy γ_{ISF} and on the elastic forces of the two partials. Specifically, the force balance consists of three terms. These are two attractive forces originating from the ISF itself and from the screw components of the two partials, balanced at equilibrium by a third repulsive force due to the edge components of the two

partials. Experimentally, γ_{ISF} is usually calculated using the following equation [12,20]

$$\gamma_{\text{ISF}} = \frac{Gb_p^2}{8\pi d} \left(\frac{2-\nu}{1-\nu}\right) \left(1 - \frac{2\nu\cos(2\theta)}{2-\nu}\right) , \tag{3}$$

where G and ν are the shear modulus and the Poisson's ratio of an fcc metal, respectively. b_p is the magnitude of the Burgers vector of the Shockley partials. d is the measured distance separating the two Shockley partial dislocations. θ, the character angle, is the angle between the line direction of the perfect dislocation and its Burgers vector.

We apply the AIM in its two approximations: the first order axial nearest-neighbor Ising model (ANNI) and the second order axial next nearest-neighbor Ising model (ANNNI) to calculate the ISFE of fcc Ni-X random solid solutions. The detailed methodology of the AIM is explained elsewhere [16,21]. The ANNI and ANNNI models require the knowledge of the energetics of three structures, fcc, hcp and dhcp, whereupon, according to the ANNI model the $\gamma_{\text{ISF}}^{\text{ANNI}}$ is determined as

$$\gamma_{\text{ISF}}^{\text{ANNI}} = \frac{8\left(E_{hcp} - E_{fcc}\right)}{V_{fcc}^{2/3}\cdot\sqrt{3}} , \tag{4}$$

and according to the ANNNI model the $\gamma_{\text{ISF}}^{\text{ANNNI}}$ is determined as

$$\gamma_{\text{ISF}}^{\text{ANNNI}} = \frac{4\left(E_{hcp} + 2E_{dhcp} - 3E_{fcc}\right)}{V_{fcc}^{2/3}\cdot\sqrt{3}} , \tag{5}$$

where E_{hcp}, E_{dhcp}, and E_{fcc} are the energies per atom of the structures hcp, dhcp and fcc, respectively, derived from supercells energetics as determined by DFT calculations. V is the volume of 4-atoms fcc unit cell, while $V_{fcc}^{2/3}\cdot\sqrt{3}$ is the area of 4-atoms in the fcc (111) plane over which the stacking fault extends.

The double hexagonal close-packed dhcp crystal structure has a 4-layer stacking pattern ABAC-ABAC and 12 atoms per conventional unit cell. dhcp, effectively, is a two hcp unit cells stacked on top of each other, but the middle layer alternates between B and C.

Given that the stacking fault is not explicitly present in the AIM, the main disadvantages of using this model is the inability to explore the change in the spatial atomic arrangement occurring near the fault and the segregation effects due to tendency of some solutes, specifically cobalt, to migrate to the fault region [22–25].

2.2. Elastic moduli calculations

The elastic stiffness constants demand knowledge of the derivative of the energy as a function of lattice strain. The calculations of the elastic constants involving a change in the volume generally results in a strong variation in the energy which can overcome the sought strain effect. To eliminate this large volume contribution to the energy, the cubic lattice can be deformed through applying volume-preserving strains. A practical procedure to reduce the numerical noise in the calculations of the two cubic elastic constants C_{11} and C_{12} is to separate the calculation of the bulk modulus B and the tetragonal shear modulus $C' = \left(C_{11} - C_{12}\right)/2$ related to the volume-preserving strain [26]. The bulk modulus of an isotropic polycrystalline aggregate of cubic crystallites is given as

$$B = \frac{C_{11} + 2C_{12}}{3} , \tag{6}$$

The tetragonal shear modulus can be determined by applying a volume-conserving orthorhombic strain tensor (ε) [26] to the cubic supercell lattice vectors

$$\varepsilon = \begin{pmatrix} x & 0 & 0 \\ 0 & -x & 0 \\ 0 & 0 & \frac{x^2}{1-x^2} \end{pmatrix} \tag{7}$$

where the total energy of the strained lattice is an even function of the distortion parameter x

$$\Delta E(x) = \Delta E(-x) = V(C_{11} - C_{12})x^2 + O[x^4] , \tag{8}$$

The third cubic elastic constant C_{44} can be determined through applying a volume-conserving monoclinic strain tensor (ε) to the cubic supercell lattice vectors

$$\varepsilon = \begin{pmatrix} 0 & \frac{x}{2} & 0 \\ \frac{x}{2} & 0 & 0 \\ 0 & 0 & \frac{x^2}{4-x^2} \end{pmatrix} \tag{9}$$

where the total energy dependence has the form

$$\Delta E(x) = \Delta E(-x) = \frac{1}{2}VC_{44}x^2 + O[x^4] , \tag{10}$$

The distortion parameter x varies between 0 and 0.05. In a completely isotropic cubic crystal, the shear modulus G is

$$G = G^{iso} = C' = \left(C_{11} - C_{12}\right)/2 = C_{44} , \tag{11}$$

However, in reality, cubic single crystals are elastically anisotropic [27] *i.e.* the shear modulus G and Young's modulus E are direction-dependent. The degree of anisotropy A_G, known as anisotropy constant or shear modulus anisotropy or the *Zener anisotropy index* [28], in cubic crystals is expressed as the ratio between C_{44} and C'

$$A_G = \frac{2C_{44}}{(C_{11} - C_{12})} , \tag{12}$$

Since A_G deviates from unity in real cubic crystals, the shear modulus G is not known in terms of the elastic constants C_{ij}. In this case, one can only place rigorous bounds on G of polycrystalline aggregates of cubic crystallites. This is possible because in a polycrystalline material, the monocrystalline grains are randomly oriented, and on such a large scale they can be considered quasi-isotropic or isotropic in a statistical sense. The upper bound as derived by Voigt [29]

$$G_V = \frac{C_{11} - C_{12} + 3C_{44}}{5} , \tag{13}$$

and the lower bound as determined by Reuss [30]

$$G_R = \frac{5(C_{11} - C_{12})C_{44}}{4C_{44} + 3(C_{11} - C_{12})} , \tag{14}$$

The average shear modulus can be estimated from these strict bounds as [31]

$$G = \frac{G_V + G_R}{2} , \tag{15}$$

As expected, when the monocrystalline grains are weakly anisotropic, both bounds of G converge; in the limit of isotropic lattice ($A_G = 1$), $G_V = G_R = C' = C_{44}$. The Young's modulus E and the Poisson's ratio ν are related to B and G through

$$E = \frac{9BG}{3B + G}; \tag{16}$$

$$\nu = \frac{3B - 2G}{6B + 2G} , \tag{17}$$

In the next Section 2.3, we present the technical details related to the calculation of the elastic moduli.

2.3. Computational method

Ni-based concentrated alloys studied here are modeled as random solid solutions neglecting chemical short range order SRO. The fcc, hcp, and dhcp phases appearing in Eqs. (4) & (5) are described using 128-atom supercells. The fcc random alloys are modeled by supercells formed by $4 \times 4 \times 2$ translations of the 4-atoms fcc cubic cell, hcp random alloys are modeled by supercells formed by $4 \times 4 \times 4$ translations of the 2-atoms hcp unit cell, and dhcp random alloys are modeled by supercells formed by $4 \times 4 \times 2$ translations of the 4-atoms dhcp unit cell.

These 128-atom supercells give access to the alloy compositions: 6.25, 12.5, 18.75, and 25 at.%. For each chemical composition, the Warren-Cowley short-range order parameters [32,33] have been minimized at several nearest neighbor coordination shells to guarantee random distribution of atoms of alloy species. First-principles calculations were performed using Density-functional theory DFT [34,35]. The Projector Augmented Wave method, implemented in the Vienna Ab initio Simulation Package (VASP) [36–38], was employed to calculate the total energies and forces, using a spin-polarized scheme. The exchange–correlation (XC) energy of electrons is described in the generalized gradient approximation (GGA) using the functional parameterization of Perdew–Burke–Ernzerhof [39]. The total energy difference between the three phases was monitored through relevant convergence-tests where the PAWs energy cut-off was set to 350 eV. In the self-consistent total-energy calculations, the integration over the Brillouin zone has been done using $3 \times 3 \times 6$, $5 \times 5 \times 2$, and $5 \times 5 \times 2$ Monkhorst–Pack k-point mesh for the $4 \times 4 \times 2(\times 4$-atoms) fcc, $4 \times 4 \times 4(\times 2$-atoms) hcp, and $4 \times 4 \times 2(\times 4$-atoms) dhcp supercells, respectively. The convergence tests for the number of the **k**-points and plane-wave cutoff were essential to assure valid total energy differences. While relaxing the fcc supercells, we did not perform shape relaxations; the translation vectors of the supercells remained unchanged – strictly no lattice distortions, which preserved the symmetry of the underlying lattice. This was done in order to enforce the macroscopic symmetry persisting in alloy, which would be otherwise gone once the microscopic symmetry is revoked in the calculation. Therefore, the fcc phase total energy was minimized by allowing only volume and local atomic relaxations, assuming a zero pressure environment. Concerning the hcp and dhcp phases, only local atomic relaxations of the supercells were performed at the corresponding fcc equilibrium volume-per-atom and at a fixed hcp ideal c/a ratio. This warrants that (a_{hcp}, c_{hcp}) and (a_{dhcp}, c_{dhcp}) correspond to the underlying fcc lattice *i.e.*, $a_{hcp}/a_{fcc} = a_{dhcp}/a_{fcc} = 1/\sqrt{2}$, $c_{hcp}/a_{fcc} = \sqrt{4/3}$ and $c_{dhcp}/a_{fcc} = 2\sqrt{4/3}$. The conjugate gradient algorithm [40] has been applied to relax the atomic positions for the three phases.

To enable the calculation of the elastic constants using first-principles methods, an fcc random alloy can be modeled using *cubic* supercells big enough to represent the chemical disorder and simultaneously allowing a realistic computational time. To this end, we constructed 108-atom cubic supercells, specifically, these are $3 \times 3 \times 3$ translations of the 4-atoms fcc cubic cell. The specific size of the supercells allows access to these alloy compositions: 6.48, 12, 18.5 and 25 at. %, which are very close to the alloy compositions of the 128-atom supercells employed to study the γ_{ISF} as specified above. The bulk modulus B was determined using a numerical equation of state (**gibbs**[41] code) provided a set of volume-energy data derived from the fcc supercells.

A real random fcc alloy is macroscopically large, thus it has a perfect cubic symmetry due to extremely effective averaging related to its large size and to the number of local configurations in this alloy. Since the modeling supercells are finite in size, they do not correspond exactly to the macroscopically large real random alloy. Hence, the strain–energy response to distorting a particular axis of the cubic supercell may not be unique. Consequently, one has to permute the rows of the strain tensors (7) and (9), and perform all the associated calculations to provide the required averaging. The final C_{11}, C_{12}, and C_{44} are the averages of those calculated from Eqs. (6), (8) and (10). Although this will increase considerably the number of calculations per each alloy composition, it is necessary to obtain average values of the elastic constants as these averages are expected to be close to the macroscopically large real random alloy values. While calculating the total energies corresponding to the strained supercells, only local atomic relaxations were allowed.

3. ISF in nickel binary alloys

For pure fcc Ni, our AIM+DFT 0 K simulations predicts γ_{ISF}^{Ni} to be 138.5 mJ/m^2 (ANNI) and 132.74 mJ/m^2 (ANNNI), which fairly agree with the room temperature RT experimental estimation 120–130 mJ/m^2[42]. Benyoucef et al. [43] concluded based on Refs. [42, 44] that a good approximation of the RT ISF energy of pure Ni is 130 ± 10 mJ/m^2. The alias shear deformation method combined with direct DFT 0 K calculations [45] obtained γ_{ISF}^{Ni} to be 132.1–137 mJ/m^2, while the supercell approach containing the stacking-fault in conjunction with direct DFT 0 K calculations [46] predicted 127.2 mJ/m^2.

The composition variation of the ISF energy due to alloying Ni matrix with a TM solute is presented in Fig. 1. The first thing to notice is the remarkable sensitivity of the ISF energy to the type of solute added and its composition. The solutes considered here produce a continuous decrease as a function of x, the atomic fraction of the solute added, except for Pd, Pt, Au, Mo, W, and Re. The ISF energy slightly changes (Pd) or increases (Pt and Au), increases at the composition 12.5 at.% Mo relative to the 6.25 at.% Mo value (in the ANNNI approximation), and slightly changes at the composition 12.5 at.% W(Re) relative to the 6.25 at.% values (ANNNI). Qualitatively, the ISFE compositional variation delivered by the ANNI and ANNNI approximations is similar except for the systems Ni-Mo, Ni-W, and Ni-Re. Quantitatively, the difference in magnitude between the ANNI and ANNNI results varies depending on the alloying element and composition.

The general decline in the ISF energy is consistent with the available experimental and theoretical observations made on some Ni alloys in the literature [25,44,46–49]. Chandran et al. [46], using direct DFT calculations in conjunction with the Supercell method and axial Ising model reported a decrease in the ISF energy upon adding cobalt to the nickel matrix. Employing cluster expansion (CE) method within the axial Ising model, similar decline trend in the composition variation of the ISF energy was observed by Dodaran et al. [49] for the Ni-base fcc random solid solution systems Ni-Al, Ni-Co, Ni-Ti, Ni-Cr. Shang et al. [45] used a combined scheme consisting of alias shear deformation and direct DFT to study the effect of several TM one-atom solute on the Ni matrix, where all the studied solutes were found to decrease the stacking fault energy.

It can be observed from the different compositional variations present in Fig. 1 that the effect of chemistry on reducing the ISF energy is highly pronounced across the d series. To see how different the change in ISF energy can be due to adding different solutes by a specific composition x, we plot in Fig. 2 the change in the ISF energy, as determined by the ANNNI approximation, upon alloying Ni with 6.25 at.% of each solute across the 3d, 4d, and 5d series; the composition 6.25 at.% is chosen because all the relevant solutes considered here are soluble when added to the Ni matrix by this amount. The results reveal that the largest reductions in the ISF energy at this particular alloy composition correspond to adding Mo, Re, Cr, Tc, and W. Within this context, it is important to draw a comparison with cobalt due to the critical role it plays when added to Ni-superalloys in causing matrix dislocation $a/2\langle 110\rangle\{\bar{1}11\}$ dissociation and the associated stacking fault formation. When compared to Mo-Re-Cr-Tc-W effect on the ISF energy produced at 6.25 at.%, cobalt has to be added by more than 12.5 at.% to achieve a comparable decrease. The requirement to increase the amount of cobalt relative to other solutes in order to obtain a low γ_{ISF} is seen in a tensile creep experiment performed at 998 K/630 MPa on polycrystalline Ni-base superalloys [50], where matrix dislocation dissociation could only occur when cobalt content was 15 or 23 wt%. No matrix dislocation dissociation was observed in the sample containing low cobalt content (5 wt%), the dislocation dissociated at γ/γ' interface where the partial dislocation sheared the γ' precipitates during secondary and tertiary creep stages. In the high cobalt content (15 or 23 wt%) Ni-base superalloys samples, the partial dislocations swept out the matrix and γ' precipitates creating extended stacking faults or deformation microtwins. The matrix dislocation dissociation
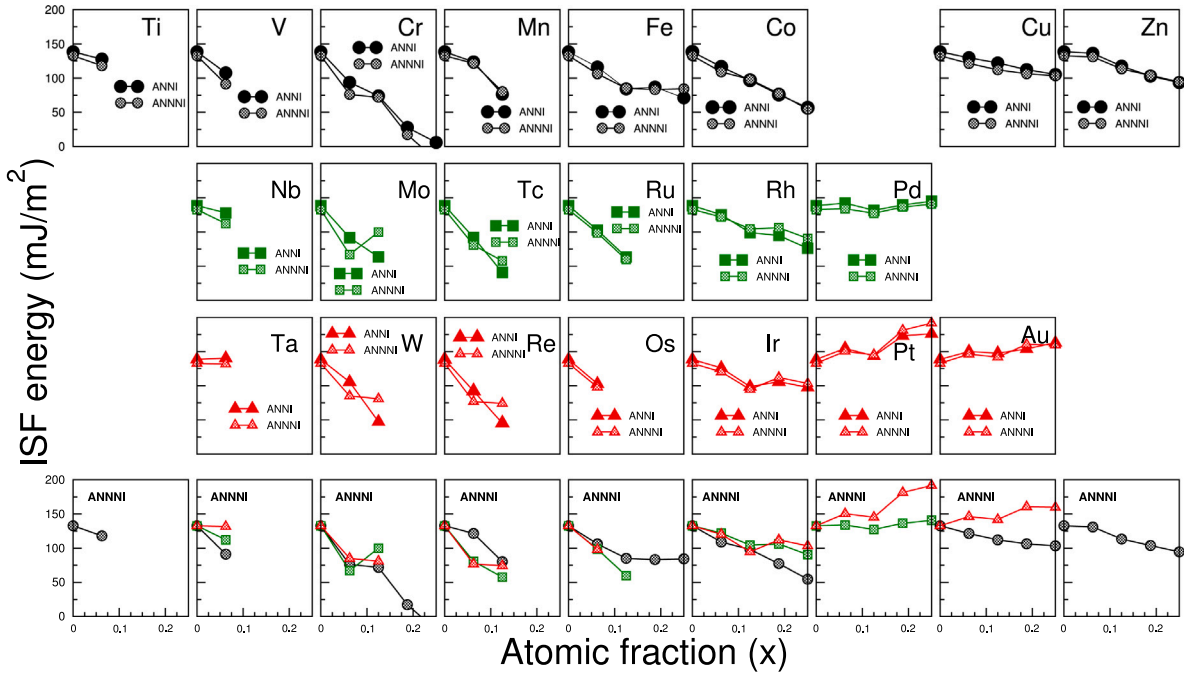
Fig. 1. The variation of ISF energy as a function of atomic fraction of the solute element x obtained using the ANNI and ANNNI approximations of the AIM.
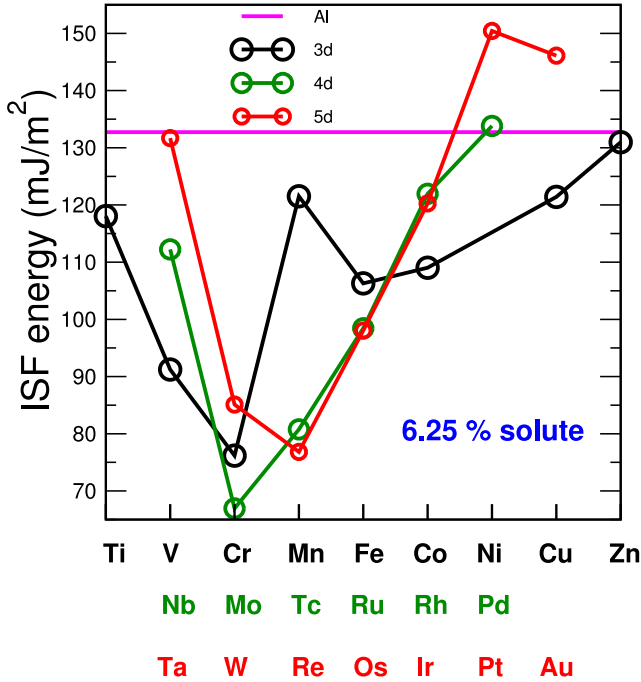

Fig. 2. Curves illustrating the variation of the ISF energy γ_{ISF} across $3d$, $4d$, and $5d$ series due to alloying Ni with 6.25 at.% X, where X is a TM element. The results correspond to the ANNNI approximation.

Table 1
Rate of change of ISF energy in Ni-X random solid solutions due to solute X as derived from the data present in Fig. 1 (ANNNI). Unit is $\frac{\text{mJ}}{\text{m}^2 \cdot \text{at.\%}}$.

Solute	$G^{\text{Ni}}_{\text{solute}}$	
	Simulation	Experiment
Pt	2.38	NA
Au	1.09	NA
Pd	0.29	NA
Ta	−0.16	NA
Ir	−1.07	NA
Cu	−1.18	NA
Rh	−1.60	NA
Zn	−1.65	NA
Fe	−1.91	NA
Ti	−2.35	NA
Co	−3	−2.37136[a]
Nb	−3.28	NA
Mn	−4.20	NA
W	−4.20	NA
Re	−4.70	NA
Os	−5.55	NA
Cr	−5.81[b]	NA
Ru	−5.84	NA
Tc	−6.00	NA
V	−6.64	NA
Mo	−10.52[c]	NA

[a] Derived from the RT exp. data [47,48].
[b] Valid up to 12.5 at.% Cr.
[c] Only compositions 0 and 6.25 at.% Mo were used in the data fitting.

and the subsequent creation of deformation microtwins, obviously due to lower stacking fault energy (SFE), improved the creep resistance resulting in a longer creep life when compared to low cobalt content (5 wt%) Ni-base superalloy sample.

The compositional variation of the intrinsic stacking fault formation energies for the binary alloys shown in Fig. 1 is generally linear, which allows a linear fit of the data yielding a gradient G_i for each system. G_i is the change in ISF energy $d\gamma_i^{Ni}$ (mJ/m^2) per an infinitesimal composition change dx_i (in atomic fraction) of solute i added to Ni,

and x_i is the solute's atomic fraction. G_i of various binary systems are presented in Table 1 in units of $\frac{\text{mJ}}{\text{m}^2 \cdot \text{at.\%}}$.

3.1. Ni-Co alloy

Cobalt plays a traditional role in reducing the stacking fault energy in Ni-superalloys. When added to Ni, Co is not susceptible to form SRO and thus the variation in ISFE is solely related to the change of Co composition in a chemically-disordered alloy. Beside our AIM+DFT
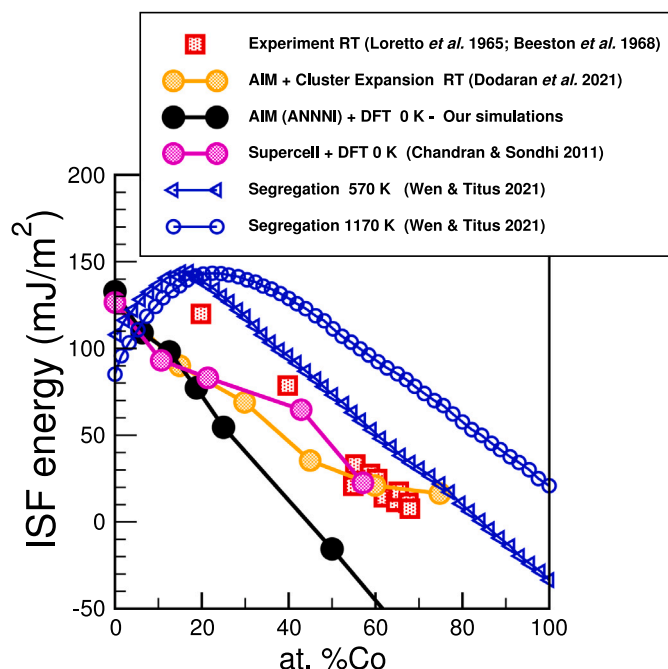
Fig. 3. Variation of the ISFE in the binary alloy Ni-Co as a function of Co composition. Also shown a comparison with RT experiment data [47,48](red squares) and other computational methods (data designated in orange circles [49] predicted at RT and in purple circles [46] at 0 K, blue triangles and circles [25] are obtained at 570 and 1170 K, respectively). (For interpretation of the references to color in this figure legend, the reader is referred to the web version of this article.)

results, other theoretical predictions obtained using the supercell approach [46] and a combined approach [49] consisting of AIM, Monte Carlo (MC), and cluster expansion (CE) method, are presented in Fig. 3. As seen in Fig. 3, our 0 K calculations slightly agree with the RT experimental data [47,48] in the Ni-rich high fault energy regime. If we accept a linear interpolation between the experimental data and in spite of the fluctuations of the experimental data in the low fault energy regime, we find our predicted rate of change of the γ_{ISF} to be different from the experiment by 0.62 $\frac{mJ}{m^2 \cdot at.\%}$. The fluctuations in the experimental data is related to the fcc-to-hcp martensitic transformation as cobalt composition approaches the RT transition value ($\sim$ 65 at.% Co) [51]. One can notice that the difference in γ_{ISF} between our simulations and the experiment increases as the cobalt composition increases. This composition-dependent difference is not observed between the Ericsson model calculations (at 570 K), which accounts for cobalt segregation to the fault region, and the experiment (RT), γ_{ISF} rate of change appears to match that of the experiment. Considering the fact that the calculations done by Ref. [25] at 1170 K yielded an increase in γ_{ISF} values, it is expected that RT data following Ericsson model would be much closer to the experiment. In fact, Ref. [25] predicted using Monte Carlo simulations cobalt to always segregate to the innermost two planes of the intrinsic stacking fault across all fcc matrix compositions but to markedly different extents. The segregation was found to increase with cobalt increasing concentration until peaking near equiatomic composition before it decreases thereafter. This behavior was observed in the studied intermediate-high temperature range 773–1173 K, where the extent of segregation is much pronounced as temperatures decreased. This can help explain the difference in γ_{ISF} rate of change between our calculations and the experiment, given that our AIM+DFT calculations do not involve solute Suzuki-segregation to the ISF region. Within this context, it is interesting to point out the variation of γ_{ISF} in the dilute limit as presented by the Ericsson model calculations [25], where the ISF energy increases markedly rather than decreasing between 0 and $\sim$ 20 at.% Co at 570 and 1150 K, featuring a peak centered around 20 at.% Co. Unfortunately, there is no experimental data within the composition range 0–20 at.% Co to confirm the validity of this unusual increase in γ_{ISF}. The observation of partial dislocations sweeping out

the matrix and γ' precipitates and creating extended stacking faults in Ni-base superalloys [50] when added by $\sim$ 15 or 23 at.%, indicates that cobalt additions does reduce the ISF energy. However, it is difficult to make conclusions regarding this issue as Ni-base superalloys is a multicomponent intricate alloy where the ISF energy change cannot be accounted for solely by cobalt presence but rather by the collective interaction between all the elements present. This peculiar feature worths further investigation.

Our AIM+DFT results differ from those of the supercell+DFT [46] and AIM+CE [49] approaches at high Co compositions. In the supercell+DFT [46] the chemical disorder is not properly accounted for. The supercell used contains three faults and comprises 56 atoms. It is specified in their study [46] that four random configurations were used to model the perfect and the faulted structures at each Co composition considered. These four distinct configurations were generated through a simple procedure consisting of randomly replacing Ni atoms with Co until the desired concentration is achieved. This is not a proper representation of the chemical disorder. The ISF energy is sensitive to the local chemistry especially when the supercell size is small. The local chemistry and the small size of the supercell used have an important effect on the ISF energy variation, which is clearly observed as cobalt concentration increases.

Concerning the AIM+CE results [49], the technique used consisted of generating 1000 atomistic configurations (by Monte Carlo sampling scheme) per each parent structure for each composition where the energy was calculated by CE. It is possible that the atomistic configurations detected in their study as the lowest energy configurations have a certain degree of chemical SRO. γ_{ISF} (Ref. [49] used the ANNNI approximation) is sensitive to the local chemistry and thus the use of configurations with SRO makes a difference. This can explain the continuous reduction in the ISFE rate of change, predicted by the AIM+CE, as cobalt composition increases. It is worth mentioning that in the AIM+CE study the energies of the small clusters (10 atoms) used to fit the effective cluster interaction are obtained by DFT calculations without accounting for local atomic relaxations. Nevertheless, this is unlikely to be the reason for the difference between our AIM+DFT and the AIM+CE γ_{ISF} results in the high Co compositions region since
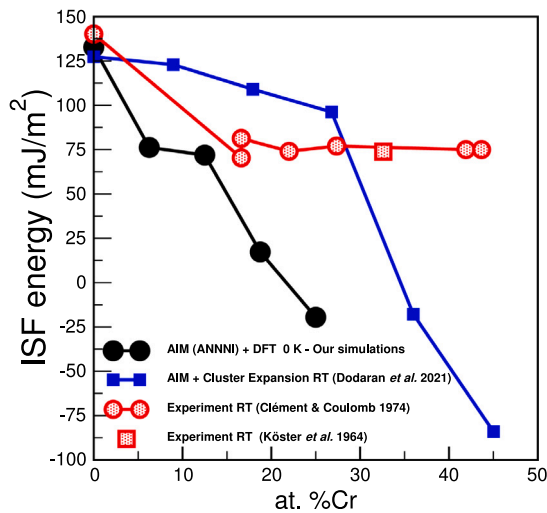
Fig. 4. Curves showing the variation of the ISFE in the alloy system Ni-Cr. Our 0 K simulations data are represented in black solid circles, while RT experimental data are designated in red circles [44] and a red square [52]. Also shown a comparison with RT computational data obtained using Cluster Expansion method combined with AIM [49]. (For interpretation of the references to color in this figure legend, the reader is referred to the web version of this article.)

the size mismatch of Ni and Co is small. It is important to mention in this context that though the γ_{ISF} curve of the AIM+CE crosses the experiment data at 60 at.% Co, the AIM+CE and the experimental γ_{ISF} composition variations qualitatively differ (from 25 at.%Co onward). While the experimental γ_{ISF} data continue to vary linearly heading towards zero around 68 at.% Co, the AIM+CE γ_{ISF} curve progressively reduces its rate of change and appears to start leveling off at 16.5 mJ/m^2 as approaching the composition 75 at.% Co.

3.2. Ni-Cr alloy

Fig. 4 presents the variation of the intrinsic stacking fault formation energy γ_{ISF} in Ni-Cr concentrated solid solution based on our random alloy modeling, alongside the RT experimental findings [44,52]. Also shown, the theoretical prediction of Ref. [49] using a combined scheme consisting of AIM, Monte Carlo, and cluster expansion method. Our calculations predict a linear decline of the γ_{ISF} as Cr concentration increases.

One can notice the qualitative and quantitative difference between our results and the experiment when Cr concentration exceeds ∼ 16 %. The γ_{ISF} reported in the experiment develops a plateau where it appears to be stabilized around the value 75 mJ/m^2 between the concentrations ∼ 16 % and ∼ 43 %, at least as given by the available experimental data. Unfortunately, other than 0 at.% Cr there is no experimental data below the 16 at.% Cr composition. It is possible that γ_{ISF} decreases rapidly between 0 and ∼ 16 % and remains constant at around 75 mJ/m^2 afterwards.

The leveling-off of γ_{ISF} at a particular value in the experimental data [44,52] is directly associated with a short range order SRO phenomena taking place in the concentrated solid solution at the relevant composition range. The remarkable difference between our results and the experiment, specifically for concentrations higher than ∼ 16 at.% Cr, is directly related to the fact that our simulations do not account for chemical SRO which appears to have a strong effect on γ_{ISF} in the Ni-Cr system as revealed by the RT experimental data [44,52].

In many substitutional solid solutions, the solute atoms do not occupy the pertinent lattice sites in a random fashion, but rather many possible correlation between the alloying atoms are observed,

giving rise to a SRO structure which is distinguished from the periodic-ordering in long range ordered LRO structures. The temperature interval within which SRO is observed is system-dependent, usually it occurs between low-medium and high temperature range. Below a critical temperature, typically low or medium, LRO or phase-decomposition occurs. Various diffuse neutron wide-angle and X-ray scattering experiments have studied the SRO phenomena in fcc Ni-Cr alloys, in the temperature range 741 to 1073 K, and confirmed its existence at these chemical compositions 11 [53], 20 [54,55], 25 [56], and 33 [56,57] at.% Cr. The diffuse intensity maxima due to SRO were always found at $(1\frac{1}{2}0)$ reciprocal lattice points which is one of the four special points of an fcc alloy. At the stoichiometric alloy composition Ni$_2$Cr (∼ 33 at.% Cr) LRO of Pt$_2$Mo-type structure, characterized by superstructure vector (2/3 2/3 0) in the reciprocal space, has been found at temperatures lower than 863 K – see Karmazin. [58] and references therein. Recently, Rahaman et al. [59] using first-principles calculations found that D1$_a$ phase should be stable for alloy compositions close to 20 at.% Cr at low temperatures, but above the Curie temperature. Though this phase is almost as stable as Ni$_2$Cr (Pt$_2$Mo), it has been suggested that it is not experimentally observed because the driving force for atomic ordering is substantially weaker [59].

Though the γ_{ISF} predicted by the AIM+CE [49] generally decreases as a function of increasing Cr content, its decline is different from our prediction. Specifically, The γ_{ISF} compositional variation obtained by the AIM+CE displays two different decline trends. It is characterized by a small decline rate in the composition range 0–27 at.% Cr followed by a drastic drop. As previously mentioned in Section 3.1, in the AIM+CE study [49], 1000 atomistic configurations were generated by Monte Carlo sampling scheme per each parent structure for each composition where the energy was calculated by CE. It is possible that the lowest energy atomistic configurations selected in the AIM+CE [49] and used to evaluate γ_{ISF} (using the ANNNI approximation) contain an important degree of chemical SRO as this energetically favorable in the case of Ni-Cr alloy system - we demonstrated above the tendency of Cr to form SRO when mixed with Ni. This is a plausible explanation accounting for the difference between our AIM+DFT chemical-disorder modeled γ_{ISF} and the weakly decreasing AIM+CE γ_{ISF} in the composition range 0–27 at.% Cr. It is equally important to point out in this regard that local atomic relaxations in the Ni-Cr alloy system cannot be neglected. We previously mentioned in Section 3.1 that in the AIM+CE study [49] the energies of the 10 atomic clusters used to fit the effective cluster interaction are obtained by DFT calculations neglecting local atomic relaxations. The size mismatch of Ni and Cr atoms is not negligible, this can have an important effect on the total energies of the phases involved in the γ_{ISF} Eq. (4) & (5) which are sensitive to energy variations. Forcing the atoms to occupy their ideal lattice sites causes strain-induced interactions which can affect the energies of the 10 atomic clusters and consequently the CE derived energies of the parent lattices (fcc,hcp,dhcp) and γ_{ISF}.

3.3. Ni-Re alloy

Rhenium manifests a weak ordering tendency when mixed with nickel. This has been reported in a diffuse X-ray scattering technique experiment done by Schönfeld et al. [60] on Ni-9.4 at.% Re alloy composition at 873 K. According to the experiment, the strength of the ordering tendency is weak and not well pronounced as implied by the rather small negative value of the α_{110} Warren-Cowley SRO parameter, making the type of the local order impossible to identify. On the other hand, recently, Ref. [61] using Monte Carlo simulations found a strong ordering tendency of the type (1 1/2 0) to exist in the alloy composition Ni-9 at.% Re. This pronounced ordering caused a phase separation transition, leading to the precipitation of a D1$_a$ ordered structure in the Ni matrix at about 940 K. Nevertheless, the authors do acknowledge that their calculated atomic SRO is much stronger than the experimental. This overestimation of the ordering tendency
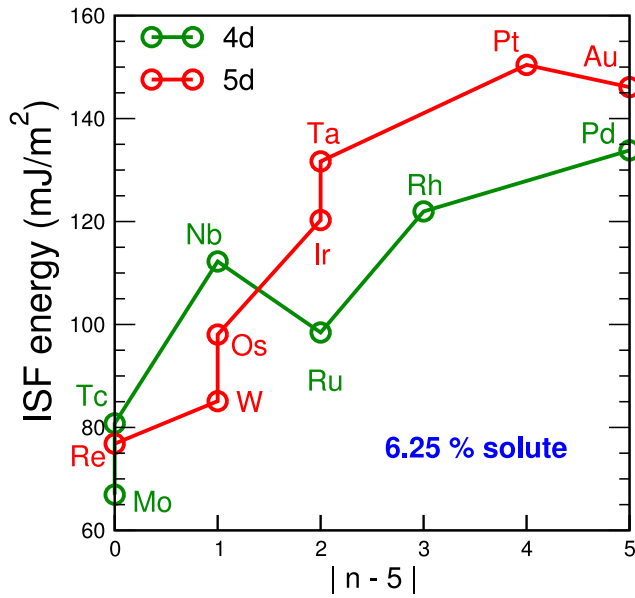
Fig. 5. Curves illustrating the evolution of ISF energy γ_{ISF} as a function of solute X $| n-5 |$ electrons count, where n is the d-electrons count of solute X. The data correspond to the ANNNI approximation.

is caused by the oversimplified description of the high-temperature state of Ni-Re and corresponding effective interactions in the current applied theories [61]. Rhenium clustering can be safely ruled out from playing any role affecting ISFE since extended X-ray absorption fine structure (EXAFS) experiment [62] found Re atoms to be exclusively surrounded by Ni atoms in binary Ni-Re system. Moreover, an atom probe tomography (APT) study [63] of Re distribution in binary Ni-Re alloy and in CMSX-4 superalloy found no evidence for Re clustering. Hence, given the weak SRO and absence of Re clustering in fcc Ni-rich Ni-Re alloys as discussed above, the ISFE compositional variation within the range 0–12.5 at. %Re (Ni-Re panel in Fig. 1) obtained using chemically-disordered supercells is expected to qualitatively agree with the experiment.

3.4. *d-band filling dependence*

The γ_{ISF} data plotted in Fig. 2 present an interesting feature, a dependence of the γ_{ISF} on the position of the solute in the d-band series. The γ_{ISF} of the 4d, and 5d band series exhibit a concave-like variation where the minimum appears to be centered around the half d-band filling solutes. Alloying Ni with solutes lying away from the half d-band filling positions produces a smaller decrease in γ_{ISF} to different extents, where the smallest reductions correspond to solutes located at the end of each d series studied here. This trend seems to be correct even for the 3d series, though the curve is interrupted by an abrupt change at Mn position due to its magnetic nature. Let us note here that some solutes located at the d series peripheries, namely Pd, Pt, and Au, even induce an increase in γ_{ISF}. This dependence of γ_{ISF} on the solute position within the periodic table can be seen more clearly if the results are displayed as a function of the absolute value of the solute d-electrons count (n) relative to the half d-band number *i.e* $| n - 5 |$. Excluding Nb from the data, the curves in Fig. 5 manifest a monotonous increase with the solute $| n - 5 |$ electrons count. Consequently, the potency of solutes to reduce the nickel matrix γ_{ISF} when added by a specific concentration is clearly related to their d-electrons count, where the maximum reduction is produced by half d-band filling solutes Re-Tc-Mo-Cr. This assumption is valid at low temperature given that our calculations are done at 0 K, though we speculate that the solute d-electrons count dependence is probably independent of temperature.

4. ISF energy of Ni-based multicomponent γ-phase alloys

Chromium and cobalt are heavily used in Ni-based multicomponent alloys. In Section 3.2, it was shown that the experimental ISFE composition variation in the alloy system Ni-Cr is not linear over the whole composition range due to chemical SRO. Cobalt is not prone to form SRO when mixed with Ni, however, it appears that Co tends to order when mixed with other solutes. Recently, experimental studies [67,68] confirmed the existence of chemical SRO in equiatomic medium entropy alloy (MEA) NiCoCr where Cr atoms were found to favorably bond with Ni and Co.

Though the chemical SRO phenomena in model and industrial γ-phases of Ni-based multicomponent alloys has been studied and confirmed, in the temperature range (25–1000 °C), long time ago in various experimental investigations [69–73], the precise role of each of the hardening elements in SRO was not identified, due to the complexity of the chemical composition of the γ-phase. However, favorable occurrence of Ni-Cr pairs was greatly emphasized to dominate the SRO microregions [71]. In single crystal NiCr-based γ-phase alloys containing different hardening elements (Mo,Co,Re,Ru, or W) [71,72], heat treated for 100 h at 1330 °C and subsequently air cooled, the intensity of SRO scattering was found well defined and unchanged up to 600 °C and slightly declined before reaching 700 °C. Between 700 and 1000 °C, SRO decreased gradually and disappeared almost completely at 1000 °C. In all the probed samples, SRO was found to exist in microregions of dimensions 5–10 Å characterized by $(1\frac{1}{2}0)$ diffuse maxima peaks.

Table 2 presents ISF energies of various NiCr-based multicomponent γ phase alloys as measured by the experiment [43,64,65], and arranged as a function of increasing cobalt composition in the γ-phase. Table 3 presents the ISFE of three Ni-base superalloys as determined experimentally by Cui et al. [66]. Unfortunately, the corresponding γ phase chemical composition is not available. However, it can be seen that the ISFE decreases gradually with increasing Co content in these Ni-superalloys. The ISFE values (40.1 ± 1.2, 33.3 ± 0.9, 24.9 ± 0.5 mJ/m^2) lie close to those reported in Table 2. As only Co and Ni concentrations are changing in the alloys (U720Li,TMW-2,TMW-4M3,TMW-26) [65] present in Table 2 – the compositions of the other solutes remain almost similar – a comparison can be made regarding Co effect on the γ_{ISF}. Though γ_{ISF} declines with increasing Co content, the rate of change (−1.15 $\frac{mJ}{m^2 \cdot at.\%}$) is not big. This is about half the value derived from the experimental data [47,48] of the binary chemically-disordered Ni-Co alloy in Fig. 3 (∼ -2.37 $\frac{mJ}{m^2 \cdot at.\%}$). Such reduction can originate from Co preference to bond with other atoms in an organized fashion when present in NiCr-based γ-phase multicomponent alloys. This observation is in accordance with the recently experimentally established existence [67,68] of chemical SRO in MEA NiCoCr where Cr atoms were observed to preferentially bond with Ni and Co. Within this context, it is worth noting that γ_{ISF} of the equiatomic MEA NiCoCr alloy is 22 ± 4 mJ/m^2[74] which is close to that of the γ-phase of TMW-4M3 (19.9 ± 2.5 mJ/m^2) NiCoCr-base superalloy [65]; this proximity is not surprising given that the chemical compositions are relatively similar.

Concerning Re effect, though it manifests a weak tendency to order in the binary Ni-Re system [60], recent experimental observations [75] showed that Re addition to a single crystal Ni-based matrix alloy leads to an increase of the chemical SRO degree as compared to a lower SRO in a similar matrix alloy containing 0 at.% Re. Thus, the weak tendency of Re to order in the binary Ni-Re system [60] becomes significant in a multicomponent γ-phase alloy, possibly due to Re preference to pair with other solutes.

Below we try to rationalize the difference in γ_{ISF} between random and SRO solid solutions. In pure crystals and in random concentrated solid solutions, the ISFE is the energy required for the leading partial of the dissociated dislocation to displace the atoms in the plane, the ISFE thus corresponds only to modify locally the atomic layers stacking sequence. When local chemical SRO exists in an alloy, the creation

Table 2

Chemical compositions in atomic % of various multicomponent γ phase alloys [43,64,65] and the corresponding experimental ISFE (γ) as measured at RT. The alloys are arranged as a function of increasing Co content. ISFE unit is in mJ/m^2.

Alloy	Ni	Cr	Co	Mo	W	Re	Ru	Al	Ti	Ta	γ(Exp.)
γMCRu [64]	65.88	26.07	–	2.03	1.98	–	4.04	–	–	–	31 ± 3
γMCRe [64]	65.60	26.21	–	2.02	1.98	4.19	–	–	–	–	32 ± 3
γ_mMC2 [43]	54.62	26.04	9.15	2.78	4.16	–	–	2.74	0.24	0.28	31
U720Li [65][a]	46.6	28.9	19.8	2.7	0.5	–	–	1.2	0.3	–	35.9 ± 3.7
TMW-2 [65][b]	38.3	27.4	29.8	2.6	0.6	–	–	0.9	0.4	–	23.4 ± 3.1
TMW-4M3 [65][c]	34.6	27.1	34.0	2.5	0.5	–	–	0.9	0.4	–	19.9 ± 2.5
TMW-26 [65][d]	36	24.8	34.7	2.4	0.6	–	–	1.0	0.5	–	27.3 ± 1.7

[a] Contains 0.002 at.% C,0.0001 at.% B,0.005 at.% Zr.

[b] Contains 0.004 at.% C,0.0001 at.% B,0.005 at.% Zr.

[c] Contains 0.003 at.% C,0.0001 at.% B,0.006 at.% Zr.

[d] Contains 0.004 at.% C,0.0001 at.% B,0.005 at.% Zr.

Table 3

Nominal chemical composition of different Ni-base superalloys in weight % as given in Ref. [66] and the corresponding experimental ISFE (γ). Unit of ISFE is in mJ/m^2.

Alloy [66]	Ni	Cr	Co	Mo	W	Al	Ti	B	Zr	C	Ce	γ(Exp.)
Alloy1	69.025	14	5	2.8	1.2	2.3	5.6	0.015	0.03	0.02	0.01	40.1 ± 1.2
Alloy2	68.025	14	15	2.8	1.2	2.3	5.6	0.015	0.03	0.02	0.01	33.3 ± 0.9
Alloy3	60.025	14	23	2.8	1.2	2.3	5.6	0.015	0.03	0.02	0.01	24.9 ± 0.5

of the stacking fault by the leading partial involves disruption of the SRO near the fault plane. The lattice of the alloy being in a low energy SRO state will resist reducing its chemical order. This adds a substantial energy penalty for the leading partial to create the fault. Hence, the ISF energy of a local chemical SRO state alloy is always higher than a complete chemical disorder state alloy. This explains why the experimental ISFE of γ-phase NiCr-based multicomponent alloys (Table 2) is constantly positive, and characterized by a small decline rate as Co composition increases.

Other than increasing γ_{ISF} value, SRO was shown to stabilize γ_{ISF} as temperature increases. Ref. [64] examined the variation of γ_{ISF} as a function of deformation temperature in two single phase γ alloys γ_{MCRe} and γ_{MCRu}; for both alloys γ_{ISF} did not deviate from the RT (298 K) measured values (32 ± 3 mJ/m^2 for γ_{MCRe} and 31 ± 3 mJ/m^2 for γ_{MCRu}) and remained constant until 1023 K. It slightly decreased when measured at 1323 K (27±3 mJ/m^2 for γ_{MCRe} and 25 ± 3 mJ/m^2 for γ_{MCRu}).

5. Elastic properties of nickel binary alloys

5.1. Elastic stiffness constants

The response of nickel-rich binary alloys to each of the applied strain appears to vary depending on the type of solute as shown in Fig. 6(a-d). Os exhibits the highest resistance to uniaxial strain (C_{11}) followed by Re, Ru, and W. While C_{11} values of Mo and Co compositions fluctuate around pure nickel, adding Ta and Fe to the Ni matrix weakens its resistance to uniaxial strain. Concerning the resistance to C_{12} the biaxial strain, Os, Re, Ru, and W, similarly to C_{11} composition variation, have a stiffening effect. As opposed to their role in affecting the resistance to uniaxial strain (C_{11}), Mo, Ta, and Fe increase C_{12} to varying extents. Co addition to the Ni matrix, similarly to C_{11} case, has insignificant effect on the resistance to biaxial strain. As for the pure shear elastic constant C_{44}, as shown in Fig. 6(c) C_{44} is stiffened upon alloying fcc Ni with close-packed solutes (Co,Os,Ru,Re) whereas it is softened upon alloying with body-centered cubic bcc solutes (Fe,W,Mo,Ta).

As shown in Fig. 6(c,d), the addition of Fe, W, Mo, and Ta clearly has softening effect on both of pure shear C_{44} and tetragonal shear (C') moduli of the nickel matrix, where Ta appears to play the prominent role in this regard at the composition 6.48 at.%. The compositional variation of C' shows a general decrease, except for Co, Os, and Ru. Re appears to reduce C', albeit weakly. C' is the stiffness associated with a shear in $\langle 110 \rangle$ direction on a plane, and in certain martensitic

transformations, the softening of this modulus as the alloy composition increases is a precursor of a phase transition [76,77]. The softening of C' predicted in Fig. 6(d) is connected with the appearance of the ordered phases Ni8Ta [78], Ni4W [79], Ni4Mo [80], and Ni3Fe [81] in the respective phase diagrams. Within this context, Ni4Re phase is reported to be stable between 0 and ∼ 930 K [82]. The phase fcc Ni-Co is thermodynamically stable over a wide composition range, up to ∼ 65 at.% Co at room temperature [51] where it undergoes a martensitic transformation to the hcp phase.

The softening induced by the elements Fe, W, Mo, and Ta is caused by their body centered cubic bcc ground state crystal structure. First-principles total energies calculations have shown that in case fcc lattice is the thermodynamically most stable phase, a hypothetical bcc lattice is usually dynamically unstable where Born stability conditions ($C_{11} + 2C_{12} > 0$, $C_{11} - |C_{12}| > 0$, $C_{44} > 0$) [84] are violated. Specific to our study, $C' < 0$ for hypothetical fcc Ta [85], (W,Mo) [85,86], and ferromagnetic Fe [87]. Embedding these bcc elements into the close-packed fcc Ni lattice weakens its resistance against shearing which is clearly reflected in the softened pure shear C_{44} and tetragonal shear C' curves in Fig. 6(c,d). Despite the softening effect of these bcc elements, the fcc alloys (Ni-Fe,Ni-W,Ni-Mo,Ni-Ta) are elastically stable within the composition range studied here since they satisfy Born stability criteria.

On the other hand the most stable thermodynamic structure of the elements Os, Co, Ru, and Re is the hexagonal close-packed hcp phase. $C' > 0$ for hypothetical fcc (Os,Ru) [88], Co [87], and Re [89]. The immersion of these hcp elements into the fcc Ni matrix does not have the effect produced by the bcc elements on the shear moduli C' and C_{44}. C' slightly changes for Co, Os, and Ru, while it decreases for Re additions but still the decrease is much less pronounced than Fe (considering the whole composition), W, Mo, and Ta. The compositional variation of C_{44} exhibits a stiffening effect when alloying fcc Ni with hcp solutes (Co,Os,Ru,Re). C_{44} stiffens the most upon Os (6.48 at. %Os) and Co (at higher concentrations) inclusions.

Though both shear moduli are reduced upon alloying with (Fe, W, Mo, Ta), C_{44} decreases at smaller rates than C'. The difference between the compositional variation of C_{44} and C' is more visible and qualitatively different when alloying with Co, Os, Ru, and Re. This higher magnitude of C_{44} and its lower decrease rate (Fe,W,Mo,Ta) or increase (Co,Os,Ru,Re) upon alloying relative to C' is caused by a higher energy penalty associated with pure shearing (C_{44}) of the anisotropic Ni-matrix lattice.
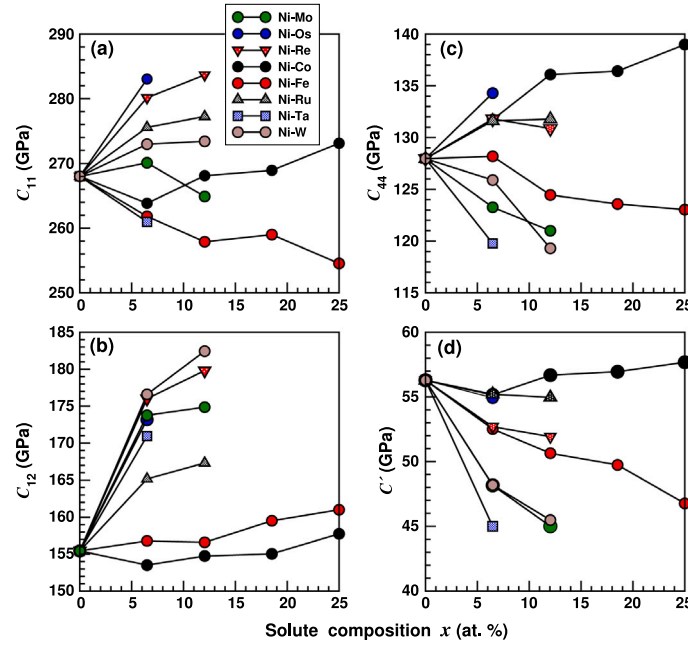
Fig. 6. Single crystal elastic constants C_{11}, C_{12}, C_{44}, and tetragonal shear modulus C' evolution as a function of alloy composition x in fcc Ni-X binaries. The experimental 0 K values [83] of fcc Ni are 261 GPa (C_{11}), 151 GPa (C_{12}), 132 GPa (C_{44}), and 55 GPa (C').

5.2. Polycrystalline elastic moduli

The shear modulus G of an ensemble of anisotropic nickel alloy crystals obtained through averaging the single crystal elastic constants is shown in Fig. 7(a). G varies in magnitude upon alloying within a range (~ 80–97 GPa) higher and lower than that of the single crystal tetragonal shear modulus C' and pure shear modulus C_{44}, respectively. The compositional dependence of G resembles to a large extent that of C_{44}, namely for the increase tendency upon alloying with Os, Ru, and Co. Rhenium is seen to reduce G similarly to its effect on C', though very slightly.

As for the bulk modulus B, the resulting change shown in Fig. 7(b) due to alloying manifests a clear dependence on the bulk moduli of the alloying elements. Generally, solutes with B bigger than that of Ni increase B of the nickel binaries, noting that the experimental B of these solutes are 424.6 (Os), 368.8 (Re), 317.7 (Ru), 312.3 (W), 264.7 (Mo), 193.7 (Ta), 193 (Co) and 169.8 GPa (Fe) [90,91].

The evolution of the polycrystalline Young's modulus E as a function of the alloy composition in Fig. 7(c) is qualitatively similar to that of G where close-packed solutes (Os,Ru,Co) increase and bcc solutes (Fe,W,Mo,Ta) decrease E of the Ni matrix to varying extents.

The variation of the anisotropy constant or *Zener anisotropy index* A_G in Fig. 7(d) shows that alloying increases the degree of elastic anisotropy of fcc nickel. This is also observed in the increase of the Poisson's ratio ν in Fig. 8. Cobalt addition appears to slightly change the elastic anisotropy of fcc Ni as demonstrated by the weak composition dependence of A_G and zero change of ν in Ni-Co binary alloy.

The maximum reduction in G (relative to the fcc Ni value of 92 GPa) in Fig. 7(a) due to alloying is 12 % (for 6.48 at.% Ta), ~ 12 % (~ 12 at.% Mo or W), ~ 9 % (25 at.% Fe) and the maximum increase is ~ 6% (25 at.% Co). This is a small change when compared to the drop in the ISFE induced by these solutes (excluding Ta) in Fig. 1. In fact, at the lowest composition (6.25 at. %) of the solutes considered in Fig. 7 the ISFE of the nickel matrix is reduced by 18–42 %. Therefore, though both γ_{ISF} and G determine the magnitude of the dislocation dissociation width d in Eq. (3), the increase in d relative to pure Ni value upon alloying is mainly attributed to the significant drop in γ_{ISF}. The dominant role played by the γ_{ISF} in increasing the stacking fault width d is expected to be even more pronounced in a Ni-based
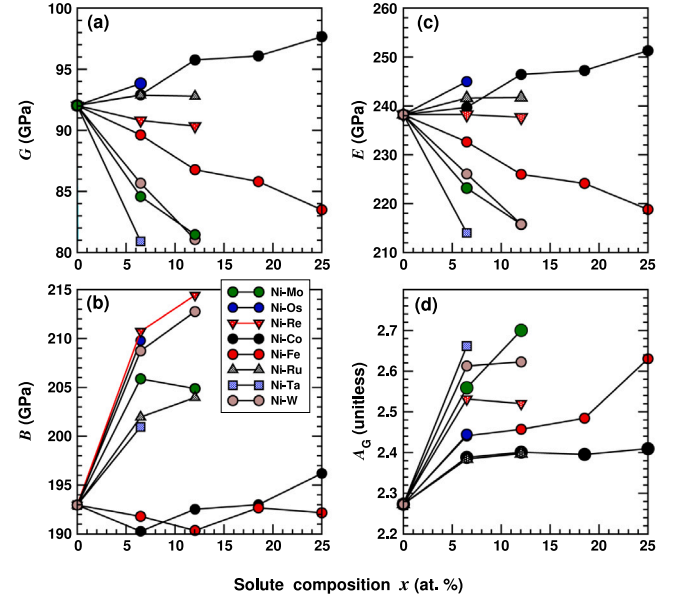

Fig. 7. Polycrystalline elastic moduli G, B, and E (panels a-c) and anisotropy constant A_G (panel d) variation as a function of alloy composition x of Ni-X binaries. The experimental values of polycrystalline G, B, and E for fcc Ni measured at 55 K are 91, 199, and 237 GPa [92].

multicomponent γ phase alloy. This is because some of the solutes in Fig. 7(a) affect G differently, while they all, except Ta, substantially decrease γ_{ISF} in Fig. 1.

6. SRO/ISFE effects on mechanical properties and outlook

Given the discussed presence of SRO in Ni-base superalloys in Section 4, it is important to emphasize its controlling-role of the deformation micromechanism, and how it affects the mechanical properties as a consequence. Post mortem TEM observations of samples deformed macroscopically show that, between 25 and 750 °C, the
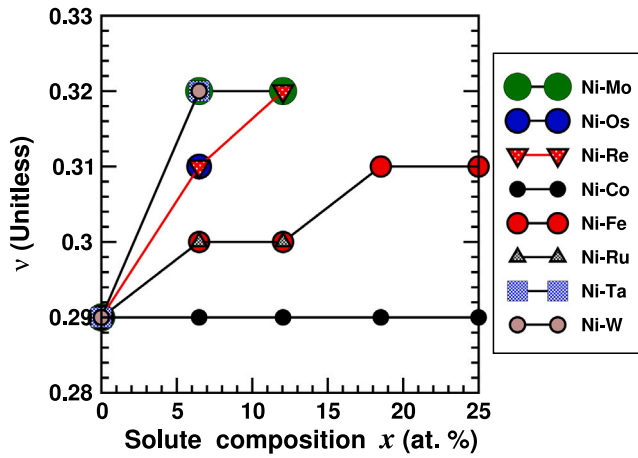
Fig. 8. Curves illustrating the evolution of the Poisson's ratio ν as a function of alloy composition x of Ni-X binaries. The Poisson's ratio ν of fcc Ni measured by the experiment at 55 K is 0.301 [92].

dislocation microstructure is mainly characterized by high localization of the deformation [71]. The collective movement of the dislocations in form of pile-ups, which controls the deformation micromechanism in NiCr-based multicomponent γ-phase, has been shown to be related to SRO-induced friction stresses [70] existing within SRO high-friction zones. The deformation evolves through the propagation of dislocation pile-ups where the two leading dislocations within the pile-ups are observed to be paired [70,71,93]. This pairing is directly connected with chemical SRO and attributed to diffuse antiphase boundary DAPB present in the material whose energy induces the linking of the two dislocations [71,94,95]. A further in situ deformation under loading [71] showed that SRO-zones friction stresses slows down and stops the head of the dislocation pile-up which consequently reduces the distances between the dislocations. The reduced inter-dislocation distances configuration creates high stress allowing the leading pair to glide past the friction zone obstacle which basically happens through destroying the SRO-formed bounds pairs such as Ni-Cr within the SRO region. The passage of the leading pair reduces the friction stresses; this glide softening effect [96] causes the inter-dislocation distances within the pile-up to increase. Between 750 °C and 900–1050 °C, the dislocation deformation microstructure gradually changes from localized-heterogeneous (dislocation pile-ups) to nonlocalized and becomes completely homogeneous (individual dislocations) marking the disappearance of the SRO hardening-role around 1050 °C in Re and Ru, and around 900 °C in W containing NiCr-based multicomponent γ-phase alloys. It is well established that SRO hardens and improves the mechanical properties of Ni-based γ-phase alloys at low-intermediate temperatures. The high friction stresses within SRO regions oppose dislocations glide and consequently induce a local shear resistance higher than the critical resolved shear stress [69,70]. Newly, a computational study on Ni-10 at.% Al [97] found cross-slip activation barriers to depend on the overall state of SRO in the alloy and on the absence/presence of a DAPB in the slip plane, suggesting that the effect of SRO on cross-slip is likely a major factor underlying mechanical behavior beyond the yield point for concentrated binary and chemical complex FCC alloys [97].

In addition to the improvement of mechanical properties induced by the SRO hardening role of the γ-phase, low stacking-fault energy has profound advantageous effects. Lowering the SFE of γ-phase facilitates dislocation dissociation and promotes the formation of deformation microtwins (microtwinning process) in Ni-base superalloys [50]. These deformation microtwins are involved in diffusion-mediated reordering, their presence is associated with an increase in the creep resistance and improvement of the creep properties of Ni-base superalloys. A

substantially low ISFE correlates with very low or even negative magnitude of the fcc→hcp structural energy difference, which can enable upon straining the fcc phase to transform locally within the matrix to the hcp phase. This local process, known as transformation-induced-plasticity (TRIP) effect, can increase the steady high strain-hardening rates and as a consequence yields high ductility and tensile strength as observed experimentally in Ni-Co-Cr medium entropy alloy [98]. Generally speaking, low ISFE affects the mechanisms of plastic deformation and is experimentally observed to be directly related to toughness, high strength, and ductility in crystalline concentrated alloys. However, as we previously discussed, hardening elements added to NiCr-based alloys are involved in SRO – specifically Co, Re, W, and Mo, though each one strengthens the chemical ordering state to a different extent – which results in an increase in the ISFE relative to the hypothetical fully chemical disordered state. Due to the local chemical SRO characterizing the γ-phase of NiCr-based multicomponent alloys, the ISFE can be reduced significantly only when a solute of preference, for instance Co in Table 2, is added in a big concentration, without the risk of precipitation of creep-strength deteriorating topologically-close packed phases [99–104]. In principle, ISFE can be tuned, desirably substantially decreased, when specific solutes characterized by significant ISFE decline rates also are insusceptible to or weakly involve in the local chemical SRO existing in the alloy; this will have the beneficial effect of tailoring the local chemical SRO in a way to keep it present but at the same time having the smallest ISFE possible. In this regard, it is interesting to single out Os, specifically because it has not received much attention as a potential hardening solute in Ni-base superalloys designed so far, as our simulations predict it to produce a high ISFE decline rate ($\sim 5.55 \frac{\text{mJ}}{\text{m}^2 \cdot \text{at.\%}}$) along with W, Re, Cr, Ru, Tc, V, and Mo when mixed with nickel. It is not known whether Os develops chemical SRO upon mixing with Ni or with other relevant solutes. Throughout the whole chemical composition range, Os does not form any ordered phase when mixed with Ni [105], which indicates that its ordering tendency can be either absent or weak, similarly to Re. While finalizing the writing of our research a new experimental work [17] appeared demonstrating that replacing Re by Os in the commercial CMSX-4 Ni-based single crystal superalloy yields a creep strain rate, at 980 °C/200 MPa/100 h, lower than the actual Re-containing CMSX-4 superalloy. This newly designed Re-free Os-containing, the so called CSU-Os-2 superalloy, even manifests phase stability better than the CMSX-4 after exposure at 1100 °C for 1000 h. The authors [17] argue that the enhanced solid solution strengthening, microstructure stability and creep resistance as compared to CMSX-4 can be explained by higher partition coefficient between γ and γ′ phases and, very likely, lower diffusion coefficient of Os than Re in γ-phase. We should emphasize here that low ISFE plays an important role as well in improving the mechanical properties of Ni-base superalloys, potentially increasing the resistance to medium-high temperature creep [106]. The high ISFE decline rate of Os can be an essential role giving rise to the attractive mechanical properties and performance of this newly developed Ni-base superalloy.

A lower twinning stress σ_T of fcc alloys is associated with lower ISFE γ_{ISF} and higher shear modulus G [107]

$$\sigma_T = K \left(\frac{\gamma_{\text{ISF}}}{Gb} \right)^{1/2} . \tag{18}$$

Os low ISFE decline rate, and high shear Modulus ($G = 256.81$ GPa [108]), can yield a low critical resolved shear stress needed to trigger a twinning-induced plasticity (TWIP) effect and can help form hcp nano-laths under strain via a martensitic fcc→hcp local transformation [98] given its hcp native structure; which is expected to enhance relevant mechanical properties (specifically work-hardening, fracture toughness, and elongation to rupture [98,109–113]) of Ni-based concentrated alloys.

Os is the least compressible metal, experimentally admitted now, as it displays a RT bulk modulus of 405 GPa [114] compared to 384 GPa [115] for Re. Recent theoretical investigations show that Os

has ideal strengths and moduli larger than those of Re and Ru [116]; specifically, Young (E = 636.42 GPa), shear (G = 256.81 GPa), bulk (B = 406.55 GPa) moduli and microhardness (H = 44.69 GPa) are higher than those of Re, Mo, Nb, Ta, W, Ir, and Rh [108]. According to our elastic calculations in Section 5.2, among all the solutes considered, Os produces the highest shear and Young moduli, and the highest bulk modulus (beside Re) when alloyed with fcc Ni in 6.48 at.%. Therefore, Os high ISFE decline rate, combined with its native-structure excellent mechanical properties, offer an exciting opportunity to design new multi-principal element alloys systems Ni40%Co40%Os20% – similarly to the newly developed Ni40%Co40%Ru20% [117] – and NiCoCr-FeMnOs. These two proposed alloys have the potential to present mechanical strength comparable or better than the current Ni-based fcc medium and high entropy alloys. It is an interesting possibility to explore.

7. Conclusions

Quantum mechanics based first-principles simulations were done to establish the 0 K composition variation of the intrinsic stacking fault formation energies ISFE, elastic constants and moduli in nickel binaries. The solute composition range in each binary alloy was restricted to its low-medium temperature solubility limit observed in the pertinent experimental phase diagram. The binary alloys were modeled as random solid solutions using big supercells, which allowed to access the variation in ISFE and in elastic properties due to finite compositional change of each solute. The compositional variation of the ISFE across a wide range of $3d$, $4d$ and $5d$ solutes was found to generally decrease, except for Pd, Pt and Au, where the ISFE slightly changes (Pd) or increases (Pt and Au). The individual compositional variations in ISFE substantially varies across $3d$, $4d$ and $5d$ series; adding solutes, lying towards the center of the transition metal series (Mo, V, Tc, Ru, Cr, Os, Re, W), to Ni gives rise to pronounced ISFE decline rates. The pivotal role played by chemical SRO in determining the value of ISFE in multicomponent γ phase alloys has been discussed. Alloying fcc Ni matrix with 6.48 at.% Os is shown to improve the elastic moduli more than the other solutes (Fe, W, Mo, Ta, Co, Re, Ru) considered in the elastic study. Given the crucial importance of low ISFE in improving the mechanical properties of high strength Ni-based alloys, Os predicted low ISFE decline rate combined with its intrinsic excellent elastic moduli make it a good candidate to design new multi-principal element alloys, specifically, these systems (Ni40%Co40%Os20% and NiCoCrFeMnOs) warrant experimental investigations.

CRediT authorship contribution statement

A. Breidi: Conceptualization, Formal analysis, Investigation, Methodology, Supervision, Validation, Visualization, Writing – original draft, Writing – review & editing. **J.D.T. Allen:** Data curation, Investigation, Methodology, Software, Validation, Visualization. **A. Mottura:** Conceptualization, Funding acquisition, Investigation, Project administration, Resources, Supervision, Validation, Visualization.

Declaration of competing interest

The authors declare that they have no known competing financial interests or personal relationships that could have appeared to influence the work reported in this paper.

Acknowledgments

References

[1] A. Breidi, J. Allen, A. Mottura, Acta Mater. 145 (2018) 97–108.

[2] T.B. Gibbons, B.E. Hopkins, Creep behaviour and microstructure of Ni-Cr base alloys, Met. Sci. 18 (5) (1984) 273–280.

[3] C.M.F. Rae, R.C. Reed, Primary creep in single crystal superalloys: Origins, mechanisms and effects, Acta Mater. 55 (3) (2007) 1067–1081.

[4] J. Weertman, Creep of indium, lead and some of their alloys with various metals, Trans. Met. Soc. AIME 218 (1960) 207–218.

[5] J.P. Poirier, Creep of Crystals: High Temperature Deformation Processes in Metals, Ceramics and Minerals, Cambridge University Press, Cambridge, 1985.

[6] Farghalli A. Mohamed, Terence G. Langdon, The transition from dislocation climb to viscous glide in creep of solid solution alloys, Acta Metall. 22 (1974) 779–788.

[7] Roger C. Reed, The Superalloys: Fundamentals and Applications, Cambridge University Press, 2006.

[8] Michael E. Kassner, Fundamentals of Creep in Metals and Alloys, Butterworth-Heinemann, 2015.

[9] Oleg D. Sherby, Peter M. Burke, Mechanical behavior of crystalline solids at elevated temperature, Prog. Mater. Sci. 13 (1968) 323–390.

[10] W. Roger Cannon, Oleg D. Sherby, High temperature creep behavior of class I and class II solid solution alloys, Metall. Trans. 1 (1970) 1030–1032.

[11] W.T. Read Jr., Dislocations in Crystals, McGraw-Hill, New York, 1953.

[12] Peter M. Anderson, John P. Hirth, Jens Lothe, Theory of Dislocations, third ed., Cambridge University Press, 2017.

[13] J.A Venables, The electron microscopy of deformation twinning, J. Phys. Chem. Solids 25 (7) (1964) 685–692.

[14] J.P. Dennison, R.J. Llewellyn, B. Wilshire, The creep and fracture behaviour of some dilute nickel alloys at 500 and 600 C, J. Inst. Met. 94 (1966) 130–134.

[15] J.P. Dennison, R.J. Llewellyn, B. Wilshire, The creep and fracture properties of some nickel-chromium alloys at 600 C, J. Inst. Met. 95 (1967) 115–118.

[16] P.J.H. Denteneer, W. van Haeringen, Stacking-fault energies in semiconductors from first-principles calculations, J. Phys. C: Solid State Phys. 20 (32) (1987) L883.

[17] Bensheng Wei, Yan Lin, Zaiwang Huang, Lan Huang, Kechao Zhou, Longfei Zhang, Lijun Zhang, A novel Re-free Ni-based single-crystal superalloy with enhanced creep resistance and microstructure stability, Acta Mater. 240 (2022) 118336.

[18] A. Howie, Quantitative experimental study of dislocations and stacking faults by transmission electron microscopy, Metall. Rev. 6 (1961) 467–503.

[19] Tartour, Washburn, Phil. Mag. 18 (1968) 1257.

[20] E. Aerts, P. Delavignette, R. Siems, S. Amelinckx, Stacking fault energy in silicon, J. Appl. Phys. 33 (1962) 3078.

[21] A. Breidi, J. Allen, A. Mottura, First-principles calculations of thermodynamic properties and planar fault energies in Co3X and Ni3X L12 compounds, Phys. Status Solidi b 254 (2017) http://dx.doi.org/10.1002/pssb.201600839.

[22] Hideji Suzuki, Segregation of solute atoms to stacking faults, J. Phys. Soc. Japan 17 (2) (1962) 322–325.

[23] T. Hickel, S. Sandlöbes, R.K.W. Marceau, A. Dick, I. Bleskov, J. Neugebauer, D. Raabe, Impact of nanodiffusion on the stacking fault energy in high-strength steels, Acta Mater. 75 (2014) 147–155.

[24] G.B. Viswanathan, R. Shi, A. Genc, V.A. Vorontsov, L. Kovarik, C.M.F. Rae, M.J. Mills, Segregation at stacking faults within the $\gamma\prime$ phase of two Ni-base superalloys following intermediate temperature creep, Scr. Mater. 94 (2015) 5–8.

[25] Dongsheng Wen, Michael S. Titus, First-principles study of suzuki segregation at stacking faults in disordered face-centered cubic Co-Ni alloys, Acta Mater. 221 (2021) 117358.

[26] J.M. Mehl, Phys. Rev. B 47 (1993) 2493–2500.

[27] S.I. Ranganathan, Martin Ostoja-Starzewski, Phys. Rev. Lett. 101 (2008) 055504.

[28] C. Zener, Elasticity and Anelasticity of Metals, University of Chicago, Chicago, 1948.

[29] W. Voigt, Ann. Phys., Lpz. 274 (12) (1889) 573–587.

[30] A. Reuss, ZAMM Z. Angew. Math. Mech. 9 (1) (1929) 49–58.

[31] R. Hill, Proc. Phys. Soc. A 65 (5) (1952) 349.

[32] J.M. Cowley, X-Ray measurement of order in single crystals of Cu_3Au, J. Appl. Phys. 21 (1) (1950) 24–30.

[33] B.E. Warren, X-ray Diffraction, Dover, New York, 1990.

[34] P. Hohenberg, W. Kohn, Inhomogeneous electron gas, Phys. Rev. 136 (1964) B864–B871.

[35] W. Kohn, L.J. Sham, Self-consistent equations including exchange and correlation effects, Phys. Rev. 140 (1965) A1133–A1138.

[36] P.E. Blöchl, Projector augmented-wave method, Phys. Rev. B 50 (1994) 17953–17979.

[37] G. Kresse, J. Furthmüller, Efficiency of ab-initio total energy calculations for metals and semiconductors using a plane-wave basis set, Comput. Mater. Sci. 6 (1996) 15–50.

[38] G. Kresse, D. Joubert, From ultrasoft pseudopotentials to the projector augmented-wave method, Phys. Rev. B 59 (1999) 1758–1775.

[39] John P. Perdew, Kieron Burke, Matthias Ernzerhof, Generalized gradient approximation made simple, Phys. Rev. Lett. 77 (1996) 3865–3868.

[40] W.H. Press, S.A. Teukolsky, W.T. Vetterling, B.P. Flannery, Numerical Recipes: The Art of Scientific Computing, third ed., Cambridge University Press, 2007.

[41] M.A. Blanco, E. Francisco, V. Luaña, GIBBS: isothermal-isobaric thermodynamics of solids from energy curves using a quasi-harmonic debye model, Comput. Phys. Comm. 158 (2004) 57–72.

[42] C.B. Carter, S.M. Holmes, The stacking-fault energy of nickel, Phil. Mag. A 35 (1977) 1161–1172.

[43] Mustafa Benyoucef, Brigitte Décamps, Armand Coujou, Nicole Clément, Stacking-fault energy at room temperature of the γ matrix of the MC2 Ni-based superalloy, Phil. Mag. A 71 (1995) 907–923.

[44] N. Clément, P. Coulomb, Phil. Mag. A 30 (1974) 663.

[45] S.L. Shang, C.L. Zacherl, H.Z. Fang, Y. Wang, Y. Du, Z.K. Liu, Effects of alloying element and temperature on the stacking fault energies of dilute Ni-base superalloys, J. Phys.: Condens. Matter 24 (2012) 505403.

[46] Mahesh Chandran, S.K. Sondhi, First-principle calculation of stacking fault energies in Ni and Ni-Co alloy, J. Appl. Phys. 109 (2011) 103525.

[47] M.H. Loretto, L.M. Clarebrough, R.L. Segall, Phil. Mag. 11 (1965) 459.

[48] B.E.P. Beeston, I.L. Dillamore, R.E. Smallman, Met. Sci. J. 2 (1968) 12–14.

[49] Mohammad S. Dodaran, Shengmin Guo, Michael M. Khonsari, Nima Shamsaei, Shuai Shao, A theoretical calculation of stacking fault energy of Ni alloys: The effects of temperature and composition, Comput. Mater. Sci. 195 (2021) 110326.

[50] Chenggang Tian, Guoming Han, Chuanyong Cui, Xiaofeng Sun, Effects of stacking fault energy on the creep behaviors of Ni-base superalloy, Mater. Des. 64 (2014) 316–323.

[51] T. Nishizawa, K. Ishida, The Co-Ni (cobalt-nickel) system, Bull. Alloy Phase Diagr. 4 (1983) 390–395.

[52] E.H. Köster, A.R. Thölen, A. Howie, Phil. Mag. A 10 (1964) 1093.

[53] W. Schweika, H.-G. Haubold, Neutron-scattering and Monte Carlo study of short-range order and atomic interaction in Ni$_{0.89}$Cr$_{0.11}$, Phys. Rev. B 37 (1988) 9240–9248.

[54] B. Schönfeld, L. Reinhard, G. Kostorz, W. Bührer, Short-range order and atomic displacements in Ni-20 at% Cr single crystals, Phys. Status Solidi b 148 (2) (1988) 457–471.

[55] B. Schönfeld, G.E. Ice, C.J. Sparks, H.-G. Haubold, W. Schweika, L.B Shaffer, X-ray study of diffuse scattering in Ni-20 at% Cr, Phys. Status Solidi b 183 (1994) 79–95.

[56] R. Caudron, M. Sarfati, M. Barrachin, A. Finel, F. Solal, In situ diffuse scatterings of neutrons on binary alloys, Physica B 180–181 (1992) 822–824.

[57] R. Caudron, M. Sarfati, M. Barrachin, A. Finel, F. Ducastelle, F. Solal, J. Physique I 2 (1992) 1145.

[58] L. Karmazin, Lattice parameter studies of structure changes of Ni–Cr alloys in the region of Ni$_2$Cr, Mater. Sci. Eng. 54 (1982) 247–256.

[59] Moshiour Rahaman, B. Johansson, A.V. Ruban, First-principles study of atomic ordering in fcc Ni-Cr alloys, Phys. Rev. B 89 (2014) 064103.

[60] R.I. Barabash, G.E. Ice, P.E.A. Turchi, Diffuse Scattering and the Fundamental Properties of Materials, Momentum Press, New york, 2009.

[61] Shuang He, Ping Peng, Oleg I. Gorbatov, Andrei V. Ruban, Effective interactions and atomic ordering in Ni-rich Ni-Re alloys, Phys. Rev. B 94 (2016) 024111.

[62] A. Mottura, R.T. Wu, M.W. Finnis, R.C. Reed, A critique of rhenium clustering in Ni–Re alloys using extended X-ray absorption spectroscopy, Acta Mater. 56 (2008) 2669–2675.

[63] A. Mottura, N. Warnken, M.K. Miller, M.W. Finnis, R.C. Reed, Atom probe tomography analysis of the distribution of rhenium in nickel alloys, Acta Mater. 58 (2010) 931–942.

[64] F. Pettinari, J. Douin, G. Saada, P. Caron, A. Coujou, N. Clément, Stacking fault energy in short-range ordered γ-phases of Ni-based superalloys, Mater. Sci. Eng. A 325 (2002) 511–519.

[65] Yong Yuan, Yuefeng Gu, Chuanyong Cui, Toshio Osada, Zhihong Zhong, Toshimitsu Tetsui, Tadaharu Yokokawa, Hiroshi Harada, Influence of Co content on stacking fault energy in Ni-Co base disk superalloys, J. Mater. Res. 26 (2011) 2833–2837.

[66] C.Y. Cui, C.G. Tian, Y.Z. Zhou, T. Jin, X.F. Sun, Dynamic strain aging in Ni base alloys with different stacking fault energy, in: Superalloys 2012, John Wiley & Sons, Ltd, 2012, pp. 715–722.

[67] F.X. Zhang, Shijun Zhao, Ke Jin, H. Xue, G. Velisa, H. Bei, R. Huang, J.Y.P. Ko, D.C. Pagan, J.C. Neuefeind, W.J. Weber, Yanwen Zhang, Local structure and short-range order in a NiCoCr solid solution alloy, Phys. Rev. Lett. 118 (2017) 205501.

[68] Ruopeng Zhang, Shiteng Zhao, Jun Ding, Yan Chong, Tao Jia, Colin Ophus, Mark Asta, Robert O. Ritchie, Andrew M. Minor, Short-range order and its impact on the CrCoNi medium-entropy alloy, Nature 581 (2020) 283–287.

[69] R. Glas, M. Jouiad, P. Caron, N. Clément, H.O.K. Kirchner, Order and mechanical properties of the γ matrix of superalloys, Acta Mater. 44 (1996) 4917–4926.

[70] M. Jouiad, F. Pettinari, N. Clément, A. Coujou, Dynamic friction stresses in the γ phase of a nickel-based superalloy, Phil. Mag. A 79 (1999) 2591–2602.

[71] F. Pettinari, M. Prem, G. Krexner, P. Caron, A. Coujou H.O.K. Kirchner, N. Clément, Local order in industrial and model γ phases of superalloys, Acta Mater. 49 (2001) 2549–2556.

[72] M. Prem, G. Krexner, F. Pettinari-Sturmel, N. Clément, Temperature dependence of ordering in the γ-phase of Ni-based superalloys, Appl. Phys. A 74 (2002) s1112–s1114.

[73] F. Pettinari-Sturmel, A. Coujou, N. Clément, The fluctuation of short-range order evidenced by mobile dislocations in the γ-phase of a nickel-based superalloy, Mater. Sci. Eng. A 400–401 (2005) 114–117.

[74] G. Laplanche, A. Kostka, C. Reinhart, J. Hunfeld, G. Eggeler, E.P. George, Reasons for the superior mechanical properties of medium-entropy CrCoNi compared to high-entropy CrMnFeCoNi, Acta Mater. 128 (2017) 292–303.

[75] Florence Pettinari-Sturmel, Joël Douin, Fabian Krieg, Ernst Fleischmann, Uwe Glatzel, Evidence of short-range order (SRO) by dislocation analysis in single-crystal Ni-based matrix alloys with varying Re content after creep, in: Sammy Tin, Mark Hardy, Justin Clews, Jonathan Cormier, Qiang Feng, John Marcin, Chris O'Brien, Akane Suzuki (Eds.), Superalloys 2020, Cham, 2020, pp. 253–259.

[76] Y. Tsunoda, N. Oishi, N. Kunitomi, Bulk modulus and martensitic transformation in Mn-Cu alloys, Physica B+C 119 (1983) 51–55.

[77] Göran Grimvall, Blanka Magyari-Köpe, Vidvuds Ozoliņš, Kristin A. Persson, Lattice instabilities in metallic elements, Rev. Mod. Phys. 84 (2012) 945–986.

[78] A. Nash, P. Nash, The Ni-Ta (nickel-tantalum) system, Bull. Alloy Phase Diagr. 5 (1984) 259–265.

[79] P.E.A. Turchi, L. Kaufman, Zi-Kui Liu, Modeling of Ni–Cr–Mo based alloys: Part I-phase stability, CALPHAD 30 (2006) 70–87.

[80] H. Okamoto, Mo-Ni (molybdenum-nickel), J. Phase Equilib. 12 (1991) 703.

[81] L.J. Swartzendruber, V.P. Itkin, C.B. Alcock, The Fe-Ni (iron-nickel) system, J. Phase Equilib. 12 (1991) 288–312.

[82] Sascha B. Maisel, Nils Schindzielorz, Alessandro Mottura, Roger C. Reed, Stefan Müller, Nickel-rhenium compound sheds light on the potency of rhenium as a strengthener in high-temperature nickel alloys, Phys. Rev. B 90 (2014) 094110.

[83] C. Kittel, Introduction to Solid State Physics, Wiley, New York, 1996.

[84] M. Born, K. Huang, Dynamical Theory of Crystal Lattices, Clarendon Press, Oxford, UK, 1954.

[85] L.G. Wang, M. Sob, Zhenyu Zhang, Instability of higher-energy phases in simple and transition metals, J. Phys. Chem. Solids 64 (2003) 863–872.

[86] Michael J. Mehl, Aarón Aguayo, L.L. Boyer, Romeo de Coss, Absence of metastable states in strained monatomic cubic crystals, Phys. Rev. B 70 (2004) 014105.

[87] G.Y. Guo, H. Holly Wang, Gradient-corrected density functional calculation of elastic constants of Fe, Co and Ni in bcc, fcc and hcp structures, Chinese J. Phys. 38 (2000) 949–961.

[88] Y. Wang, S. Curtarolo, C. Jiang, R. Arroyave, T. Wang, G. Ceder, L.-Q. Chen, Z.-K. Liu, Ab initio lattice stability in comparison with CALPHAD lattice stability, Comput. Coupling Phase Diagr. Thermochem. 28 (2004) 79–90.

[89] P.J. Craievich, M. Weinert, J.M. Sanchez, R.E. Watson, Local stability of nonequilibrium phases, Phys. Rev. Lett. 72 (1994) 3076–3079.

[90] Patanachai Janthon, Sijie Luo, Sergey M. Kozlov, Francesc Viñes, Jumras Limtrakul, Donald G. Truhlar, Francesc Illas, Bulk properties of transition metals: A challenge for the design of universal density functionals, J. Chem. Theory Comput. 10 (2014) 3832–3839.

[91] K. Lejaeghere, V. Van Speybroeck, G. Van Oost, S. Cottenier, Error estimates for solid-state density-functional theory predictions: An overview by means of the ground-state elemental crystals, Crit. Rev. Solid State Mater. Sci. 39 (2014) 1–24.

[92] A. Haglund, M. Koehler, D. Catoor, E.P. George, V. Keppens, Polycrystalline elastic moduli of a high-entropy alloy at cryogenic temperatures, Intermetallics 58 (2015) 62–64.

[93] M. Jouiad, N. Clément, A. Coujou, Friction stresses in the γ phase of a nickel-based superalloy, Phil. Mag. A 77 (3) (1998) 689–699.

[94] P. Schwander, B. Schönfeld, G. Kostorz, Configurational energy change caused by slip in short-range ordered Ni–Mo, Phys. Status Solidi b 172 (1992) 73–85.

[95] N. Clément, A. Coujou, Y. Calvayrac, F. Guillet, D. Blavette, S. Duval, Local order and associated deformation mechanisms in the γ phase of nickel base superalloys, Microsc. Microanal. Microstruct. 7 (1996) 65–84.

[96] V. Gerold, H.-P. Karnthaler, Acta Metall. 37 (1989) 2177.

[97] Anas Abu-Odeh, Mark Asta, Modeling the effect of short-range order on cross-slip in an FCC solid solution, Acta Mater. 226 (2022) 117615.

[98] J. Miao, C.E. Slone, T.M. smith, C. Niu, H. Bei, M. Ghazisaeidi, G.M. Pharr, M.J. Mills, The evolution of the deformation substructure in a Ni-Co-Cr equiatomic solid solution alloy, Acta Mater. 132 (2017) 35–48.

[99] R.E. Watson, L.H. Bennett, Transition-metal alloy formation – the occurrence of topologically close packed phases-I, Acta Metall. 32 (1984) 477–489.

[100] C.M.F. Rae, R.C. Reed, The precipitation of topologically close-packed phases in rhenium-containing superalloys, Acta Mater. 49 (2001) 4113–4125.

[101] B. Seiser, R. Drautz, D.G. Pettifor, TCP phase predictions in Ni-based superalloys: structure maps revisited, Acta Mater. 59 (2011) 749–763.

[102] Haibo Long, et al., Structural evolution of topologically closed packed phase in a Ni-based single crystal superalloy, Acta Mater. 185 (2020) 233–244.

[103] Huixin Jin, et al., Atomistic mechanism of phase transformation between topologically close-packed complex intermetallics, Nature Commun. 13 (2022) 2487.

[104] Sangwon Lee, Jeonghyeon Do, Kyuseon Jang, Hosun Jun, Yejun Park, Pyuck-Pa Chou, Promotion of topologically close-packed phases in a Ru-containing Ni-based superalloy, Scr. Mater. 222 (2023) 115041.

[105] T.Ya. Velikanova, T.G. Mazhuga, O.L. Semenova, P.S. Martsenyuk, V.M. Vereshchaka, Phase diagram of the Ni–Os system, Powder Metall. Met. Ceram. 41 (2002) 288–295.

[106] Young-Kwang Kim, Donghoon Kim, Hong-Kyu Kim, Chang-Seok Oh, Byeong-Joo Lee, An intermediate temperature creep model for Ni-based superalloys, Int. J. Plast. 79 (2016) 153–175.

[107] M.A. Meyers, O. Vöhringer, V.A. Lubarda, The onset of twinning in metals: a constitutive description, Acta Mater. 49 (2021) 4025–4039.

[108] Y. Sun, K. Xiong, Z. Li, S. Zhang, Y. Mao, First-principles study of structural, mechanical, and thermodynamic properties of refractory metals (Rh, Ir, W, Ta, Nb, Mo, Re, and Os), Mater. Sci. Forum 993 (2020) 1017–1030.

[109] Bernd Gludovatz, Easo P. George, Robert O. Ritchie, Processing, microstructure and mechanical properties of the CrMnFeCoNi high-entropy alloy, JOM 67 (2015) 2262–2270.

[110] Bernd Gludovatz, Anton Hohenwarter, Keli V.S. Thurston, Hongbin Bei, Zheng-gang Wu, Easo P. George, Robert O. Ritchie, Exceptional damage-tolerance of a medium-entropy alloy CrCoNi at cryogenic temperatures, Nature Commun. 7 (2016) 10602.

[111] Zijiao Zhang, Hongwei Sheng, Zhangjie Wang, Bernd Gludovatz, Ze Zhang, Easo P. George, Qian Yu, Scott X. Mao, Robert O. Ritchie, Dislocation mechanisms and 3D twin architectures generate exceptional strength-ductility-toughness combination in CrCoNi medium-entropy alloy, Nature Commun. 8 (2017) 14390.

[112] Shuo Huang, He Huang, Wei Li, Dongyoo Kim, Song Lu, Xiaoqing Li, Erik Holmström, Se Kyun Kwon, Levente Vitos, Twinning in metastable high-entropy alloys, Nature Commun. 9 (2018) 2381.

[113] Keli V.S. Thurston, Anton Hohenwarter, Guillaume Laplanche, Easo P. George, Bernd Gludovatz, Robert O. Ritchie, On the onset of deformation twinning in the CrFeMnCoNi high-entropy alloy using a novel tensile specimen geometry, Intermetallics 110 (2019) 106469.

[114] C. Pantea, I. Mihut, H. Ledbetter, J.B. Betts, Y. Zhao, L.L. Daemen, H. Cynn, A. Migliori, Bulk modulus of osmium, 4–300 K, Acta Mater. 57 (2009) 544–548.

[115] Shigeaki Ono, Equation of state determination for rhenium using first-principles molecular dynamics calculations and high-pressure experiments, Adv. Condens. Matter Phys. 2022 (2022) 7545777.

[116] Jie Wang, Jian-Ying Qi, Xian Zhou, Ideal strength and deformation-induced phase transformation of hcp metals Re, Ru, and Os: A first-principles study, Mater. Sci. Eng. A 534 (2012) 353–364.

[117] M.A. Charpagne, K.V. Vamsi, Y.M. Eggeler, S.P. Murray, C. Frey, S.K. Kolli, T.M. Pollock, Design of Nickel-Cobalt-Ruthenium multi-principal element alloys, Acta Mater. 194 (2020) 224–235.